Self-Powered, Broadband Photodetector Based on Two-Dimensional Tellurium-Silicon Heterojunction

Amirhossein Hasani,*,[+] Mohammad Reza Mohammadzadeh,[+] Hamidreza Ghanbari, Mirette Fawzy, Thushani De Silva, Amin Abnavi, Ribwar Ahmadi, Abdelrahman M. Askar, Fahmid Kabir, R. K. N. D. Rajapakse, and Michael M. Adachi*

ACCESS | 📊 Metrics & More | 📖 Article Recommendations | 🆘 Supporting Information
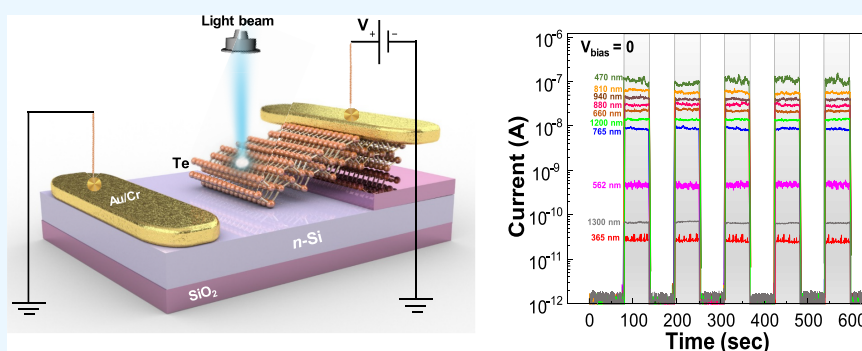
ABSTRACT: As a new class of two-dimensional (2D) materials and a group-VI chalcogen, tellurium (Te) has emerged as a p-type semiconductor with high carrier mobility. Potential applications include high-speed opto-electronic devices for communication. One method to enhance the performance of 2D material-based photodetectors is by integration with a IV group of semiconductors such as silicon (Si). In this work, we demonstrate a self-powered, high-speed, broadband photodetector based on the 2D Te/n-type Si heterojunction. The fabricated Te/n-type Si heterojunction exhibits high performance in the UV−vis−NIR light with a high responsivity of up to ∼250 mA/W and a photocurrent-to-dark current ratio (I_{on}/I_{off}) of ∼10^6, fast response time of 8.6 μs, and superior repeatability and stability. The results show that the fabricated Te/n-type Si heterojunction photodetector has a strong potential to be utilized in ultrafast, broadband, and efficient photodetection applications.

1. INTRODUCTION

Two-dimensional (2D) materials have emerged as a remarkable platform for developing a wide range of optoelectronic devices due to their unique features.[1,2] 2D materials have sparked intense interest for the fabrication of semiconductor devices since monolayer graphene nanosheets were first reported in 2004.[3] In addition, transition metal dichalcogenides (TMDs), such as WS_2, MoS_2, WSe_2, and $MoSe_2$, have gained a lot of interest as one of the most outstanding classes of the 2D material family group owing to their tremendous optical, electrical, and mechanical capabilities, sizeable bandgap, and high quantum yield for light emission.[4−8] However, there are some considerable limitations for optoelectronic applications such as the limited bandgap of graphene and relatively low carrier mobility of TMDs.[3]

2D Te, a group-VI element, has recently gained considerable interest due to several remarkable properties, such as remarkably high hole mobility, high optical absorption, high thermoelectric performance, piezoelectricity, and superior mechanical and chemical stability compared to the other high-mobility 2D materials such as phosphorene.[9,10] In 2018,

Amani et al. successfully synthesized 2D Te nanosheets.[11] Moreover, they found that 2D Te has high carrier mobility (∼1000 cm^2 V^{-1} s^{-1}) at room temperature (RT). Therefore, 2D Te has high potential for a variety of nanoelectronic devices such as high-speed field-effect transistors, photodetectors, and nanomodulators.

Photodetectors are used in a wide range of applications including biomedical devices, image processors, automatic control systems, and communication systems.[12] Photodetectors can be classified into two categories: narrowband and broadband.[13] Photodetectors that are sensitive to a broadband of wavelengths are used in a number of applications including memory storage, broadband communication, and optoelec-
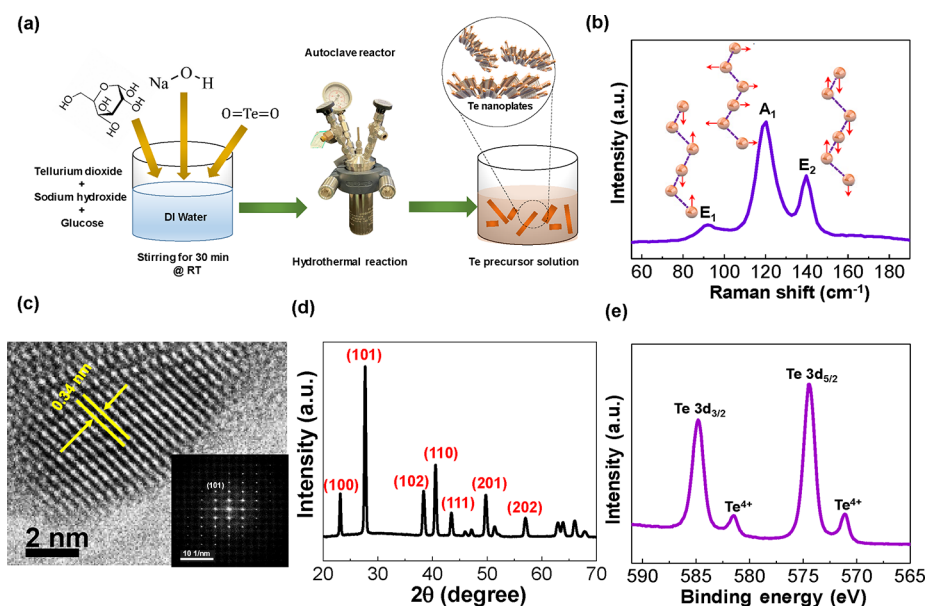
Figure 1. (a) Schematic of the hydrothermal synthesis process for Te nanoflakes. (b) Raman spectrum of the Te crystal, showing the characteristic peaks for Te (E_{1g} at 92 cm^{-1}, A_{1g} at 121 cm^{-1}, and E_{2g} at 143 cm^{-1}). (c) High-resolution transition electron microscopy (HR-TEM) image and selected area diffraction (SAED) pattern (inset) of the Te crystal. (d) XRD and (e) XPS spectra of the-as synthesized Te crystal.
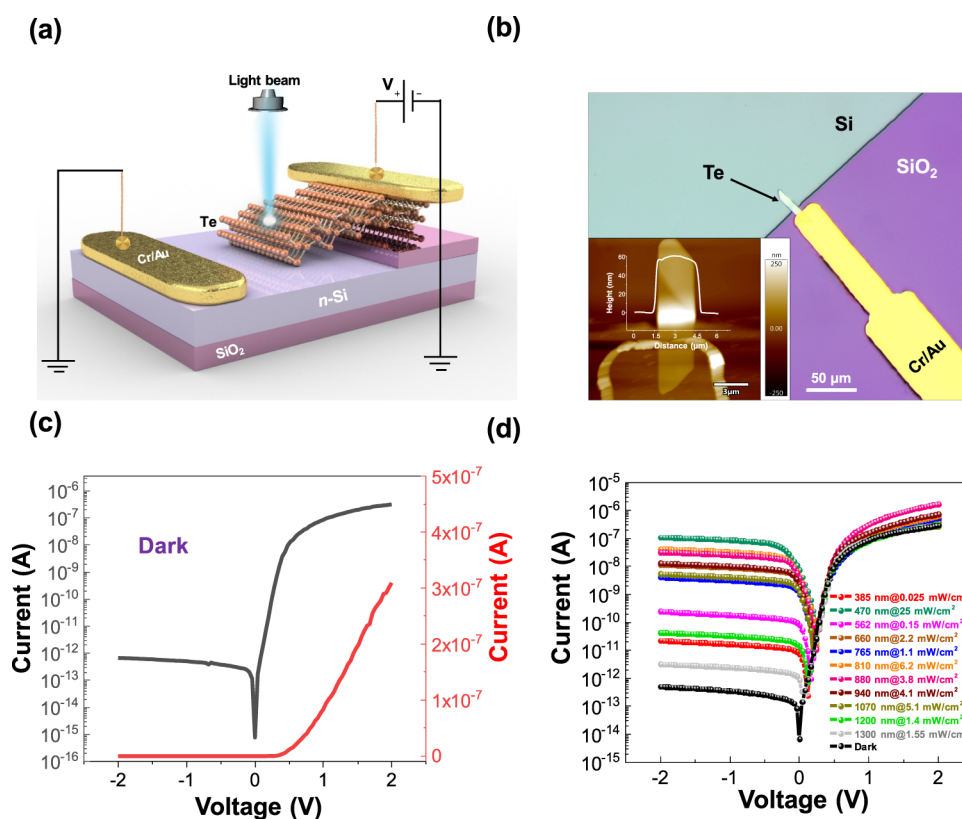
Figure 2. (a) 3D Schematic of the Te/n-Si heterojunction device. (b) Optical microscopic image of the as-fabricated device and (inset) AFM image of the as-synthesized Te nanoflake. (c) $I-V$ measurement of the heterojunction device in a dark environment and room temperature (logarithmic and linear). (d) $I-V$ curves of the device under light illumination with different power intensities and different wavelengths (from 385 to 1300 nm).

tronic systems.[13] TMDs have been frequently used in photodetection applications.[14] For instance, Lopez-Sanchez et al. fabricated a photodetector based on monolayer MoS$_2$, which shows a photoresponsivity of 880 AW^{-1} in the wavelength range of 400−680 nm.[15] In addition, Yao et al.

demonstrated a broadband photodetector based on the WS$_2$ film with a photoresponse of 0.5 AW^{-1}.[16] Despite the relatively good performance, TMD-based photodetectors are limited by low carrier mobility. Moreover, well-studied TMDs such as MoS$_2$ and WS$_2$ lack photosensitivity at wavelengths beyond
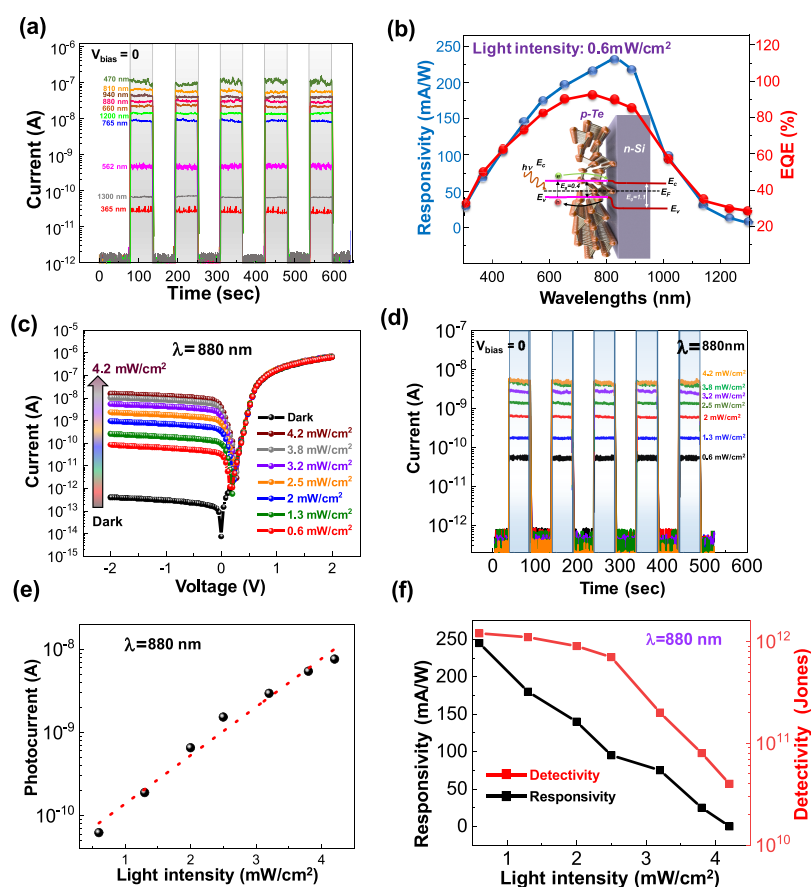
Figure 3. (a) Real-time photoresponse characteristics under illumination of light at 0 V bias with various wavelengths. (b) Responsivity and EQE of the as-fabricated Te/n–Si as a function of wavelength and (inset) band diagram of the device. (c) I−V curves and (d) photoresponse versus time of the heterojunction under different light intensities at a constant wavelength of λ = 880 nm and 0 V bias. (e) Photocurrent as a function of light intensity of the device at λ = 880 nm. (f) Responsivity and detectivity of the photodetector device versus light intensity at λ = 880 nm.

visible light and therefore have limited application in the near-infrared (NIR) spectral region. A 2D/3D heterostructure based on 2D materials and a conventional semiconductor can overcome the above disadvantages.[13,17−19] A higher optical absorption and better charge separation can be easily achieved by the integration of 2D materials and a 3D semiconductor, suggesting an enhanced photodetection efficiency. For example, Xu et al. fabricated a photodetector based on the MoS_2/GaAs heterojunction, exhibiting a very high photoresponse to vis−NIR.[20]

Herein, we demonstrated a self-powered, broadband photodetector based on the 2D Te/n-Si heterojunction. Te nanoflakes were synthesized using a modified hydrothermal process. The fabricated Te/n-type Si (n-Si) heterojunction exhibited high device performance to broadband (UV−visible-NIR) incident light at 0 bias voltage. The device showed a high responsivity of ~250 mA/W, high photocurrent-to-dark current ratio (I_{on}/I_{off}) of ~10^6, and fast rise time of 8.6 μs at an incident wavelength of λ = 880 nm at 0 V bias. The 2D Te-Si heterojunction is therefore a promising candidate for high-performance and high-speed photodetection applications.

2. RESULTS AND DISCUSSION

2D Te nanoflakes were synthesized by a hydrothermal process with glucose as a surfactant agent. In this method, TeO_2, NaOH, and glucose were used in the hydrothermal process, as illustrated in Figure 1a, during which Te nanoflakes formed

gradually in a pressurized autoclave reactor. Note that glucose was used because it is a safer alternative to hydrazine hydrate, a reducing agent conventionally used in Te synthesis.[21] The three Raman modes A_{1g}, E_{1g}, and E_{2g} at 121, 92, and 143 cm^{-1}, respectively, were observed in the Raman spectra of the 2D Te flakes, as shown in Figure 1b, which are in agreement with previous reports.[10] A high-resolution transmission electron microscopy (HR-TEM) image of the hydrothermally synthesized Te flakes is shown in Figure 1c. The lattice constant was measured to be ~0.34 nm, corresponding to the (101) plane. The selected area electron diffraction (SAED) pattern of the Te is shown in the inset of Figure 1c, in which the diffraction center corresponds to the (101) plane. Due to the anisotropic crystal structure of Te, Te grew in a (101) direction.[22]Figure 1d shows the X-ray diffraction (XRD) pattern of the Te crystal, corresponding to the hexagonal crystal structure of Te (JCPDS, 36-1452).[23] There is a dominant peak located at 27° that is attributed to the (101) plane, suggesting the high quality of the as-synthesized Te crystal. Figure 1e indicates the XPS results of the as-synthesized Te crystal. There are two strong peaks located at 584.8 and 574.4 eV, which are ascribed to Te $3d_{5/2}$ and Te $3d_{3/2}$, respectively.[21] In addition, two weak peaks were observed at 571.1 and 581.5 eV, which are assigned to Te^{4+}, and it is due to the slight oxidation of Te on the surface.[24]

The 2D Te flakes were integrated into a 2D Te-Si heterojunction device, as illustrated in Figure 2a. The top sides of the n-type Si substrate and the 2D Te flake were
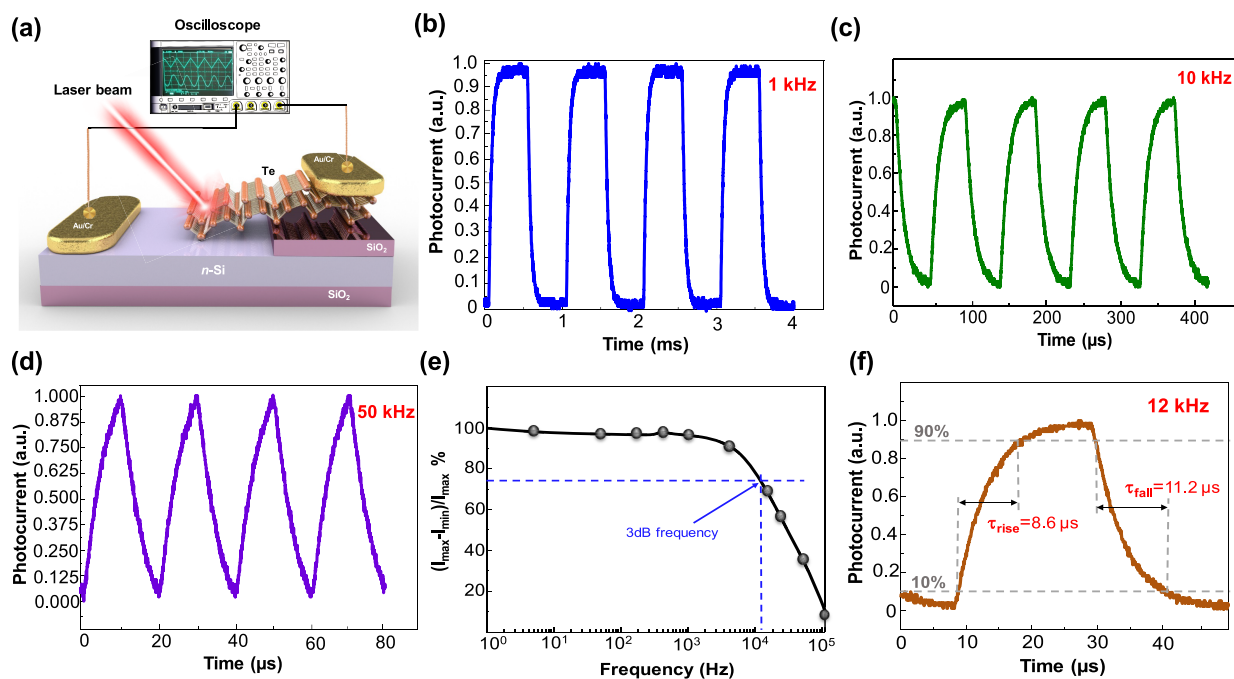
Figure 4. (a) Schematic configuration for frequency response measurements. Normalized photoresponse curves of the Te/n-Si heterojunction to an 880 nm pulsed laser at different frequencies of (b) 1 kHz, (c) 10 kHz, and (d) 50 kHz. (e) Relative response as function of frequency and (f_{3dB}). (f) Rise (τ_{rise} = 8.6 μs) and fall (τ_{fall} = 11.2 μs) time characteristics of the Te/n-Si heterojunction device.

electrically contacted using Cr/Au electrodes. The top-side thermally grown SiO_2 film (300 nm in thickness) was used to electrically isolate the Cr/Au electrode on the 2D Te flake from the n-type Si substrate. The optical microscopic image of the top view of the fabricated heterojunction device is shown in Figure 2b. The thickness of the multilayer Te flake, obtained by atomic force microscopy (AFM), was measured to be ∼60 nm (inset of Figure 2b). To identify the conduction type of the as-synthesized Te, a Te field effect transistor (FET) was fabricated. Figure S1 shows the transfer curve of Te FET, behaving like a p-type semiconductor. The current−voltage (I−V) characteristic of the Te/n-Si heterojunction under dark conditions is shown in Figure 2c. The device exhibited a high diode rectification behavior, suggesting the formation of a p−n junction across the interface of Te and n-Si. The rectification ratio, defined as the current ratio at +1 and −1 V (I_{+1V}/I_{-1V}), was >10^5 under dark conditions. The device I−V curve was measured under incident light illuminated by light-emitting diodes of different wavelengths (λ = 385, 470, 562, 660, 765, 810, 880, 940, 1070, 1200, and 1300 nm) and dark conditions, as shown in Figure 2d. The 2D Te/n-Si heterojunction exhibited an extraordinary photovoltaic effect, and the photocurrent measured at reverse bias increased by over 5 orders of magnitude between the dark conditions and the highest intensity of light (λ = 470 nm at 25 mW/cm²) (Figure 2d). The photocurrent was 8.1 × 10^{-9} at 880 nm (3.8 mW/cm²) at 0 V, representing an I_{on}/I_{off} ratio of ∼10^6. The Te/n-Si heterojunction, therefore, operates as a self-powered (i.e., photovoltaic) photodetector.

The dynamic photoresponse of the Te/n-Si heterojunction to the various wavelengths of light at zero voltage bias is shown in Figure 3a. Under zero bias (V = 0 V), the current increased from 5.5 × 10^{-12} A under a dark condition to 2.4 × 10^{-7} A at 470 nm (25 mW/cm²), representing a photocurrent-to-dark current (I_{on}/I_{off}) ratio of ∼10^5. The photodetector demon-

strated high photosensitivity over a broadband of wavelengths from 365 to 1300 nm with reproducible and stable photoresponse. The strong photoresponse at 1300 nm implies that it can be used for O-band fiber optic in optical communication applications.[25] The following expressions are used to evaluate a photodetector performance:[26]

$$\text{external quantum efficiency (EQE)} = \frac{hcR}{e\lambda} \qquad (1)$$

$$\text{responsivity } (R) = |I_{ph}/(P \times S)| \qquad (2)$$

$$\text{photocurrent } (I_{ph}) = I_l - I_d \qquad (3)$$

$$\text{detectivity } (D^*) = \frac{S^{1/2}R}{(2eI_d)^{1/2}} \qquad (4)$$

where e, c, and h are the electron charge constant, speed of light, and Planck's constant, respectively, and I_d and I_l are the dark current and light-on current, respectively. The wavelength, light intensity, and effective area are λ, P, and S (∼24 μm²), respectively. The spectral photoresponsivity of the heterojunction was determined under light illumination (λ = 350−1300 nm) at a constant intensity, as shown in Figure 3b. The Te/n-Si heterojunction photodetector exhibits a broadband photoresponse, with maximum sensitivity at approximately 880 nm, which is attributed to the highest absorption at this wavelength in the Si substrate.[13] Additionally, the EQE, shown on the secondary y axis of Figure 3b as a function of wavelength, indicates an impressive photon-to-electron conversion efficiency up to incident light wavelength of 1300 nm. The energy band diagram of the Te/n-Si heterojunction, shown in the inset of Figure 3b, represents type-II band alignment.[13] Figure 3c shows the I−V characteristic of the Te/n-Si photodetector under the different incident light intensities ranging from dark conditions to 4.2 mW/cm² at a wavelength

(a)

(b)

(c)

(d)
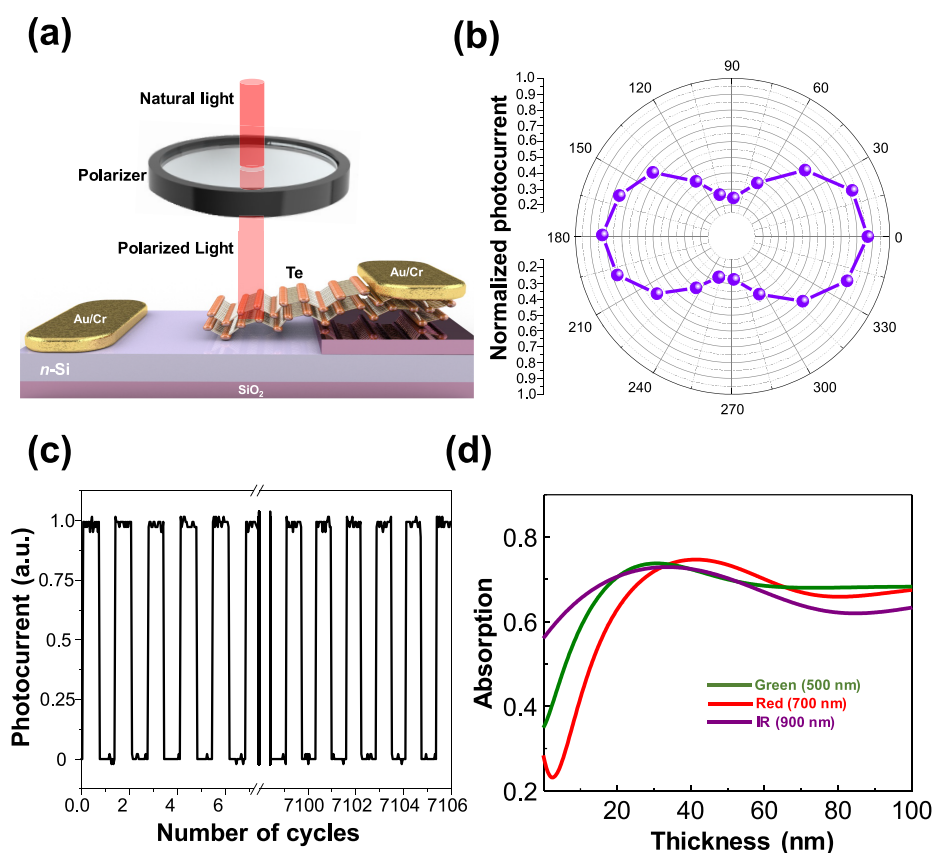
Figure 5. (a) 3D Schematic illustration of the polarization sensitivity measurement. (b) Angle-dependent normalized photocurrent of the Te/n-Si heterojunction. (c) Stability test of the as-fabricated Te/n-Si heterojunction up to about 7000 photoresponse cycles. (d) Absorption as a function of Te thickness under red, green, and IR light illumination.

of $\lambda = 880$ nm. The photocurrent increased from 1.45×10^{-14} A (dark) to 7.61×10^{-9} A (4.2 mW/cm^2) at 0 V bias. The time-response photocurrent of the device under light illumination at a wavelength of $\lambda = 880$ nm measured under different light intensities at 0 V bias is shown in Figure 3d. Even at a low light intensity of 0.6 mW/cm^2, the Te/n-Si photodetector exhibited an I_{on}/I_{off} ratio of ~100. Therefore, the photodetector is suitable for low-light condition applications. The photocurrent plotted on a log scale as a function of light intensity at a wavelength of $\lambda = 880$ nm shown in Figure 3e reveals a linear relationship for light intensities between 0.6 and 4.2 mW/cm^2. The detectivity (D^*) and responsivity (R) versus light intensity at a wavelength of $\lambda = 880$ nm are shown in Figure 3f. D^* and R increased as light intensity decreased, which is attributed to higher carrier recombination under higher light intensity.[13]

The transient response behavior of the Te/n-Si photodetector was examined by frequency response analysis. The photocurrent of the device in response to an 880 nm pulsed light-emitting diode at various frequencies was measured using an oscilloscope (Figure 4a). The normalized photoresponses under pulsed light at 1, 10, and 50 kHz are shown in Figure 4b−d, respectively. The Te/n-Si heterojunction exhibited a high 3 dB frequency (f_{3dB}) of ~12 kHz and a wide range of frequency response over 95 kHz (see Figure 4e). The rise time and fall time, defined as the time to transition from 10 to 90% of the photocurrent signal and vice versa, were measured to be 8.6 and 11.2 μs, respectively (Figure 4f), suggesting that the Te/n-Si photodetector is a promising candidate for high-speed optical communication applications. The high speed of this

photodetector is ascribed to the high carrier mobility of Te compared to other 2D material-based heterojunction photodetectors reported previously.[10,27]

Polarization sensitivity in photodetectors can increase the signal-to-noise ratio and has a variety of applications such as biomedical imaging and optical communication devices.[19,28] The Te/n-Si photodetector exhibited a remarkable response to polarized light due to the intrinsic anisotropic nature of Te. The photodetector was illuminated by polarized light with a wavelength of $\lambda = 880$ nm, as illustrated in Figure 5a. The normalized photocurrent as a function of the polarization angle of light is shown in Figure 5b, revealing that photodetector response is highly dependent on the incident polarization angle. The peak values of the photocurrent were measured at 0 and 180° polarization angles, and the minimum photocurrent values were measured at 90 and 270°, indicating a sine function with a peak-to-valley ratio of ~3. The extraordinary polarization sensitivity of the Te/n-Si heterojunction photodetector is due to the greatly anisotropic crystal structure of Te nanoflakes.[29] Figure 5c shows the cyclability and stability test of the Te/n-Si photodetector, showing a continuous response of about 7000 cycles without notable degradation in signal amplitude. The devices also have good environmental stability. A three-month exposure to the air without any encapsulation seemed not to affect the device's electrical performance (Figure S2).

The optimized Te nanosheet thickness for photon absorption was investigated using the multiple reflection interference methods, which have been developed based on Fresnel's law and adopted to many 2D materials' inter-

Table 1. Comparison of the Photodetection's Parameters of the Te/Si Photodetector and Other Photodetectors Based on 2D Materials/Si Heterojunction

device structure	wavelength range (nm)	bias voltage	responsivity	rise time/fall time	detectivity (Jones)	ref
MoS_2/Si	405−660	1−5 V	76.1 A/W	~25/48.9 s	1.6×10^{12}	36
WS_2/Si	340−1100	−5 V	5.7 A/W	670/998 μs		18
$MoTe_2$/Si	300−1800	0 V (self-powered)	0.19 A/W	150/380 ns	6.8×10^{13}	37
WSe_2/Si	200−1550	0 V (self-powered)	294 mA/W	4.1/104 μs	8.79×10^{13}	38
α-MoO_3/Si	405−1550	0 V (self-powered)	63.3 mA/W	0.47/0.76 ms	3.1	39
Graphene/$MoSe_2$/Si	365−1310	0 V (self-powered)		0.27/0.35 μs	7.13×10^{10}	40
Graphene/Si	633	2 V	0.65 A/W	1/1 ms	1.88×10^{12}	41
WO_{3-x}/$WSe2$/SiO_2/Si	900	−1.5 V	137.7 A/W	7.05/5.52 ms	2.27×10^{14}	42
WO_{3-x}/ Si	405−780	−5 V	72.8 A/W	5.8 μs/1.27 ms	3.96×10^{11}	17
Te/Si	365−1300	0 V (self-powered)	250 mA/W	8.6/11.2 μs	1.8×10^{12}	this work

faces.[11,30,31] This was employed to determine the thickness of ultrathin flakes from optical microscopic images as well as to investigate the intensity evolution of both the Raman and PL signals of 2D materials.[32−35] We investigated the light absorption of Te nanosheets deposited on Si substrates as a function of their thickness. The absorption was calculated by considering multiple reflection interference at the interfaces (air-Te-Si) and in the interlayers and the complex refractive indices of each medium in the multilayer configuration. As shown in Figure 5d, photon absorption simulations under green (500 nm), red (700 nm), and infrared (900 nm) illumination suggest that 40−60 nm is the optimal thickness for high-performance photodetectors as stronger absorption leads to enhanced photocurrent generation. Table 1 summarizes the important photodetection parameters of various photodetectors based on 2D materials/Si heterojunctions. As a result, the Te/Si heterojunction is considered advantageous to the self-powered, broadband, and high-speed photodetector.

3. CONCLUSIONS

In summary, 2D Te was synthesized by the hydrothermal process and integrated into a Te/n-Si heterojunction photodetector. The photodetector exhibited a high I_{on}/I_{off} ratio of ~10^6, EQE of 91%, responsivity of 248 mA/W, detectivity of 1.8×10^{12} Jones, fast rise and fall response times of 8.6 and 11.2 μs, respectively, at 0 V, and a broadband response up to a wavelength of λ = 1300 nm. The high-performance Te/n-Si photodetector is attributed to high electron mobility of 2D Te and type-II band alignment of the Te and Si interface. In addition, the device showed polarization sensitivity and a superior stability toward about 7000 cycles without any notable degradation in signal amplitude. Therefore, the Te/n-Si heterojunction photodetector is a promising candidate in high-speed, broadband, and efficient photodetection applications.

4. EXPERIMENTAL SECTION

4.1. Synthesis of Te Nanoflakes. NaOH (0.4 g), 0.2 g of glucose, and 0.4 g of TeO_2 were dissolved in 80 mL of DI water at RT. A homogeneous solution was obtained via 20 min of sonication of the above solution. Then, the solution was transferred to a 100 mL Teflon-lined autoclave and heated at 180 °C for 1 h. Finally, the as-synthesized hexagonal Te nanoflakes were collected and washed three times with ethanol and IPA to remove any chemical residues.

4.2. Fabrication of Te/n-Si Heterojunction. As a substrate, an n-Si wafer with a thermally grown SiO_2 layer (300 nm) was used. SiO_2/Si substrates were ultrasonically

cleaned by using a three-step cleaning process by acetone, IPA, and DI water. The substrates were then treated by Ar plasma to make them superhydrophilic. Afterward, Te precursor solution was drop-casted on SiO_2/Si substrates and baked at 100 °C. To fabricate the Te/n-Si heterojunction device, a Microposit S1813 photoresist was applied and then the photolithography process, thermal evaporation, and lift-off in an acetone bath were done to pattern electrodes with thicknesses of 10 nm Cr and 60 nm Au on the SiO_2/Si substrate. Subsequently, another photoresist layer was applied on the Cr/Au/SiO_2/Si substrate, and a window was opened to the Te crystal. To etch the SiO_2 layer and create a sloped sidewall, the sample was immersed in 3% diluted hydrofluoric acid (HF) for 30 min.

4.3. Characterization. The thickness of the Te nanoflake was evaluated by atomic force microscopy (MFP-3D, Asylum). Raman microscopy (Renishaw, 514 nm excitation laser) was used to verify the Te crystals. Transmission electron microscopy (TEM, JEOL-2100F, Japan) was employed to show the crystal structure and lattice constant. PANalytical Empyrean was used for XRD measurements using a Cu (Kα, 1.5406 Å) source. XPS examination was carried out utilizing a monochromatic aluminum source (Al K, 1486.6 eV) running at 150 W in a Kratos Analytical Axis ULTRA spectrometer with a DLD spectrometer.

4.4. Device Measurement. A probe station connected to a Keithley (SCS-4200) semiconductor measurement system, an oscilloscope (Tektronix, MDO3104, USA), a spectrometer (Thorlabs, PM100D, USA), a waveform generator, and light sources was used to perform the electrical/optical measurements.

■ ASSOCIATED CONTENT

ⓢ Supporting Information

The Supporting Information is available free of charge at https://pubs.acs.org/doi/10.1021/acsomega.2c06589.

> The transfer curve of the Te FET device and stability of the device in air (PDF)

■ AUTHOR INFORMATION

Corresponding Authors

Amirhossein Hasani − *School of Engineering Science, Simon Fraser University, Burnaby V5A 1S6 British Columbia, Canada;* ⓞ orcid.org/0000-0003-0965-4169; Email: amirhossein_hasani@sfu.ca

Michael M. Adachi − *School of Engineering Science, Simon Fraser University, Burnaby V5A 1S6 British Columbia,*

Canada; ● orcid.org/0000-0003-3015-2606;
Email: mmadachi@sfu.ca

Authors

Mohammad Reza Mohammadzadeh − *School of Engineering Science, Simon Fraser University, Burnaby V5A 1S6 British Columbia, Canada*

Hamidreza Ghanbari − *School of Engineering Science, Simon Fraser University, Burnaby V5A 1S6 British Columbia, Canada*

Mirette Fawzy − *Department of Physics, Simon Fraser University, Burnaby V5A 1S6 British Columbia, Canada*

Thushani De Silva − *School of Engineering Science, Simon Fraser University, Burnaby V5A 1S6 British Columbia, Canada*

Amin Abnavi − *School of Engineering Science, Simon Fraser University, Burnaby V5A 1S6 British Columbia, Canada*

Ribwar Ahmadi − *School of Engineering Science, Simon Fraser University, Burnaby V5A 1S6 British Columbia, Canada*

Abdelrahman M. Askar − *School of Engineering Science, Simon Fraser University, Burnaby V5A 1S6 British Columbia, Canada;* ● orcid.org/0000-0002-6092-0031

Fahmid Kabir − *School of Engineering Science, Simon Fraser University, Burnaby V5A 1S6 British Columbia, Canada;* ● orcid.org/0000-0003-3998-2753

R. K. N. D. Rajapakse − *School of Engineering Science, Simon Fraser University, Burnaby V5A 1S6 British Columbia, Canada*

Complete contact information is available at:
https://pubs.acs.org/10.1021/acsomega.2c06589

Author Contributions

[+]A.H. and M.R.M. contributed equally to this work. A.H. and M.R.M. performed all the fabrication and experimental tasks. A.H. and M.M.A. provided the project leadership and supervision. M.F. performed the AFM measurements. T.D.S. performed the Raman measurements. A.A., R.A., and H.G. assisted with the device fabrication and electrical measurements. A.M.A. performed the TEM measurements. F.K. and R.K.N.D.R. participated in the data analysis. The manuscript was written through contributions of all authors. All authors have given approval to the final version of the manuscript.

Notes

The authors declare no competing financial interest.

◼ REFERENCES

(1) Hasani, A.; Tekalgne, M.; Van Le, Q.; Jang, H. W.; Kim, S. Y. Two-dimensional materials as catalysts for solar fuels: hydrogen evolution reaction and CO_2 reduction. *J. Mater. Chem. A* **2019**, *7*, 430−454.

(2) Koppens, F.; Mueller, T.; Avouris, P.; Ferrari, A.; Vitiello, M.; Polini, M. Photodetectors based on graphene, other two-dimensional materials and hybrid systems. *Nat. Nanotechnol.* **2014**, *9*, 780−793.

(3) Shi, Z.; Cao, R.; Khan, K.; Tareen, A. K.; Liu, X.; Liang, W.; Zhang, Y.; Ma, C.; Guo, Z.; Luo, X. Two-dimensional tellurium: progress, challenges, and prospects. *Nano-Micro Lett.* **2020**, *12*, 1−34.

(4) Hasani, A.; Van Le, Q.; Tekalgne, M.; Choi, M.-J.; Lee, T. H.; Jang, H. W.; Kim, S. Y. Direct synthesis of two-dimensional MoS_2 on p-type Si and application to solar hydrogen production. *NPG Asia Mater.* **2019**, *11*, 1−9.

(5) Hasani, A.; Van Le, Q.; Tekalgne, M.; Choi, M.-J.; Choi, S.; Lee, T. H.; Kim, H.; Ahn, S. H.; Jang, H. W.; Kim, S. Y. Fabrication of a WS_2/p-Si heterostructure photocathode using direct hybrid thermolysis. *ACS Appl. Mater. Interfaces* **2019**, *11*, 29910−29916.

(6) Abnavi, A.; Ahmadi, R.; Hasani, A.; Fawzy, M.; Mohammadzadeh, M. R.; De Silva, T.; Yu, N.; Adachi, M. M. Free-Standing Multilayer Molybdenum Disulfide Memristor for Brain-Inspired Neuromorphic Applications. *ACS Appl. Mater. Interfaces* **2021**, *13*, 45843−45853.

(7) Zhao, W.; Ghorannevis, Z.; Chu, L.; Toh, M.; Kloc, C.; Tan, P.-H.; Eda, G. Evolution of electronic structure in atomically thin sheets of WS_2 and WSe_2. *ACS Nano* **2013**, *7*, 791−797.

(8) Wang, X.; Gong, Y.; Shi, G.; Chow, W. L.; Keyshar, K.; Ye, G.; Vajtai, R.; Lou, J.; Liu, Z.; Ringe, E.; Tay, B. K.; Ajayan, P. M. Chemical vapor deposition growth of crystalline monolayer $MoSe_2$. *ACS Nano* **2014**, *8*, 5125−5131.

(9) Zhou, J.; Liu, F.; Lin, J.; Huang, X.; Xia, J.; Zhang, B.; Zeng, Q.; Wang, H.; Zhu, C.; Niu, L.; Wang, X.; Fu, W.; Yu, P.; Chang, T. R.; Hsu, C. H.; Wu, D.; Jeng, H. T.; Huang, Y.; Lin, H.; Shen, Z.; Yang, C.; Lu, L.; Suenaga, K.; Zhou, W.; Pantelides, S. T.; Liu, G.; Liu, Z. Large-area and high-quality 2D transition metal telluride. *Adv. Mater.* **2017**, *29*, 1603471.

(10) Cai, X.; Han, X.; Zhao, C.; Niu, C.; Jia, Y. Tellurene: An elemental 2D monolayer material beyond its bulk phases without van der Waals layered structures. *J. Semicond.* **2020**, *41*, No. 081002.

(11) Amani, M.; Tan, C.; Zhang, G.; Zhao, C.; Bullock, J.; Song, X.; Kim, H.; Shrestha, V. R.; Gao, Y.; Crozier, K. B.; Scott, M.; Javey, A. Solution-synthesized high-mobility tellurium nanoflakes for short-wave infrared photodetectors. *ACS Nano* **2018**, *12*, 7253−7263.

(12) Dong, T.; Simões, J.; Yang, Z. Flexible photodetector based on 2D materials: processing, architectures, and applications. *Adv. Mater. Interfaces* **2020**, *7*, 1901657.

(13) Wu, E.; Wu, D.; Jia, C.; Wang, Y.; Yuan, H.; Zeng, L.; Xu, T.; Shi, Z.; Tian, Y.; Li, X. In situ fabrication of 2D WS_2/Si type-II heterojunction for self-powered broadband photodetector with response up to mid-infrared. *ACS Photonics* **2019**, *6*, 565−572.

(14) Huo, N.; Konstantatos, G. Recent progress and future prospects of 2D-based photodetectors. *Adv. Mater.* **2018**, *30*, 1801164.

(15) Lopez-Sanchez, O.; Lembke, D.; Kayci, M.; Radenovic, A.; Kis, A. Ultrasensitive photodetectors based on monolayer MoS_2. *Nat. Nanotechnol.* **2013**, *8*, 497−501.

(16) Yao, J.; Zheng, Z.; Shao, J.; Yang, G. Stable, highly-responsive and broadband photodetection based on large-area multilayered WS_2 films grown by pulsed-laser deposition. *Nanoscale* **2015**, *7*, 14974−14981.

(17) Zhang, X.; Su, Y.; Tang, Z.; Hu, D.; Wang, Z.; Hou, Y.; Wang, X. WO3-x/Si nn homotype heterojunction with high performance photodetection characteristics. *Scr. Mater.* **2020**, *189*, 89−94.

(18) Lan, C.; Li, C.; Wang, S.; He, T.; Jiao, T.; Wei, D.; Jing, W.; Li, L.; Liu, Y. Zener tunneling and photoresponse of a WS_2/Si van der Waals heterojunction. *ACS Appl. Mater. Interfaces* **2016**, *8*, 18375−18382.

(19) Xin, Y.; Wang, X.; Chen, Z.; Weller, D.; Wang, Y.; Shi, L.; Ma, X.; Ding, C.; Li, W.; Guo, S.; Liu, R. Polarization-sensitive self-powered type-II GeSe/MoS_2 van der Waals heterojunction photodetector. *ACS Appl. Mater. Interfaces* **2020**, *12*, 15406−15413.

(20) Xu, Z.; Lin, S.; Li, X.; Zhang, S.; Wu, Z.; Xu, W.; Lu, Y.; Xu, S. Monolayer MoS_2/GaAs heterostructure self-driven photodetector with extremely high detectivity. *Nano Energy* **2016**, *23*, 89−96.

(21) Yu, P.; Zhou, L.; Jia, Z.; Wu, K.; Cui, J. Morphology and property tuning of Te nanostructures in a hydrothermal growth. *J. Mater. Sci.: Mater. Electron.* **2020**, *31*, 16332−16337.

(22) Li, Z.; Zheng, S.; Zhang, Y.; Teng, R.; Huang, T.; Chen, C.; Lu, G. Controlled synthesis of tellurium nanowires and nanotubes via a facile, efficient, and relatively green solution phase method. *J. Mater. Chem. A* **2013**, *1*, 15046−15052.

(23) Manikandan, M.; Dhanuskodi, S.; Maheswari, N.; Muralidharan, G.; Revathi, C.; Rajendra Kumar, R.; Mohan Rao, G. High performance supercapacitor and non-enzymatic hydrogen peroxide sensor based on tellurium nanoparticles. *Sens. Bio-Sens. Res.* **2017**, *13*, 40−48.

(24) Tao, H.; Sun, X.; Back, S.; Han, Z.; Zhu, Q.; Robertson, A. W.; Ma, T.; Fan, Q.; Han, B.; Jung, Y.; Sun, Z. Doping palladium with tellurium for the highly selective electrocatalytic reduction of aqueous CO_2 to CO. *Chem. Sci.* **2018**, *9*, 483−487.

(25) Firstov, S. V.; Khegai, A. M.; Kharakhordin, A. V.; Alyshev, S. V.; Firstova, E. G.; Ososkov, Y. J.; Melkumov, M. A.; Iskhakova, L. D.; Evlampieva, E. B.; Lobanov, A. S. Compact and efficient O-band bismuth-doped phosphosilicate fiber amplifier for fiber-optic communications. *Sci. Rep.* **2020**, *10*, 1−9.

(26) Badahdah, H.; Kutbee, A.; Katowah, D.; Hussein, M. A.; Al-Ahmadi, N.; Altuwirqi, R.; Al-Jawhari, H. Solution processed near-infrared photodetectors using hybrid MoS_2-P (Py-co-OT) composite films. *Mater. Res. Bull.* **2021**, *138*, No. 111229.

(27) Wu, B.; Liu, X.; Yin, J.; Lee, H. Bulk *β*-Te to few layered *β*-tellurenes: indirect to direct band-Gap transitions showing semiconducting property. *Mater. Res. Express* **2017**, *4*, No. 095902.

(28) Ye, L.; Wang, P.; Luo, W.; Gong, F.; Liao, L.; Liu, T.; Tong, L.; Zang, J.; Xu, J.; Hu, W. Highly polarization sensitive infrared photodetector based on black phosphorus-on-WSe_2 photogate vertical heterostructure. *Nano Energy* **2017**, *37*, 53−60.

(29) Jia, C.; Wu, D.; Wu, E.; Guo, J.; Zhao, Z.; Shi, Z.; Xu, T.; Huang, X.; Tian, Y.; Li, X. A self-powered high-performance photodetector based on a MoS_2/GaAs heterojunction with high polarization sensitivity. *J. Mater. Chem. C* **2019**, *7*, 3817−3821.

(30) Liu, C.; Ma, Y.; Li, W.; Dai, L. The evolution of Raman spectrum of graphene with the thickness of SiO_2 capping layer on Si substrate. *Appl. Phys. Lett.* **2013**, *103*, 213103.

(31) Lien, D.-H.; Kang, J. S.; Amani, M.; Chen, K.; Tosun, M.; Wang, H.-P.; Roy, T.; Eggleston, M. S.; Wu, M. C.; Dubey, M.; Lee, S. C.; He, J. H.; Javey, A. Engineering light outcoupling in 2D materials. *Nano Lett.* **2015**, *15*, 1356−1361.

(32) Li, X.-L.; Qiao, X.-F.; Han, W.-P.; Lu, Y.; Tan, Q.-H.; Liu, X.-L.; Tan, P.-H. Layer number identification of intrinsic and defective multilayered graphenes up to 100 layers by the Raman mode intensity from substrates. *Nanoscale* **2015**, *7*, 8135−8141.

(33) Jung, I.; Pelton, M.; Piner, R.; Dikin, D. A.; Stankovich, S.; Watcharotone, S.; Hausner, M.; Ruoff, R. S. Simple approach for high-contrast optical imaging and characterization of graphene-based sheets. *Nano Lett.* **2007**, *7*, 3569−3575.

(34) Van Velson, N.; Zobeiri, H.; Wang, X. Rigorous prediction of Raman intensity from multi-layer films. *Opt. Express* **2020**, *28*, 35272−35283.

(35) Zhang, H.; Wan, Y.; Ma, Y.; Wang, W.; Wang, Y.; Dai, L. Interference effect on optical signals of monolayer MoS_2. *Appl. Phys. Lett.* **2015**, *107*, 101904.

(36) Shin, G. H.; Park, J.; Lee, K. J.; Lee, G.-B.; Jeon, H. B.; Choi, Y.-K.; Yu, K.; Choi, S.-Y. Si−MoS_2 vertical heterojunction for a photodetector with high responsivity and low noise equivalent power. *ACS Appl. Mater. Interfaces* **2019**, *11*, 7626−7634.

(37) Lu, Z.; Xu, Y.; Yu, Y.; Xu, K.; Mao, J.; Xu, G.; Ma, Y.; Wu, D.; Jie, J. Ultrahigh speed and broadband few-layer $MoTe_2$/Si 2D−3D heterojunction-based photodiodes fabricated by pulsed laser deposition. *Adv. Funct. Mater.* **2020**, *30*, 1907951.

(38) Zhang, X.; Shao, J.; Su, Y.; Wang, L.; Wang, Y.; Wang, X.; Wu, D. In-situ prepared WSe_2/Si 2D-3D vertical heterojunction for high performance self-driven photodetector. *Ceram. Int.* **2022**, *48*, 29722−29729.

(39) Zhao, S.; Liu, Y.; Wu, Y.; Liu, Y.; Guo, F.; Li, S.; Yu, W.; Liu, G.; Hao, J.; Wang, H. Self-powered broadband *α*-MoO_3/Si photodetector based on photo-induced thermoelectric effect. *Ceram. Int.* **2022**, 25079.

(40) Mao, J.; Yu, Y.; Wang, L.; Zhang, X.; Wang, Y.; Shao, Z.; Jie, J. Ultrafast, broadband photodetector based on $MoSe_2$/silicon heterojunction with vertically standing layered structure using graphene as transparent electrode. *Adv. Sci.* **2016**, *3*, 1600018.

(41) Wang, Y.; Yang, S.; Lambada, D. R.; Shafique, S. A graphene-silicon Schottky photodetector with graphene oxide interlayer. *Sens. Actuators, A* **2020**, *314*, No. 112232.

(42) Guo, T.; Ling, C.; Zhang, T.; Li, H.; Li, X.; Chang, X.; Zhu, L.; Zhao, L.; Xue, Q. High-performance $WO_{3−x}$-WSe_2/SiO_2/n-Si heterojunction near-infrared photodetector via a homo-doping strategy. *J. Mater. Chem. C* **2018**, *6*, 5821−5829.

H